



Degradation heterogeneities induced by repetitive start/stop events in proton exchange membrane fuel cell: Inlet vs. outlet and channel vs. land



Julien Durst^a, Adrien Lamibrac^{b,c}, Frédéric Charlot^d, Jérôme Dillet^{b,c},
Luis F. Castanheira^a, Gaël Maranzana^{b,c}, Laetitia Dubau^{a,**},
Frédéric Maillard^a, Marian Chatenet^a, Olivier Lottin^{b,c,*}

^a LEPMI – UMR5279, CNRS/Grenoble-INP/UdS/UJF, Saint Martin d'Hères, France

^b LEMTA, Université de Lorraine, Vandoeuvre-lès-Nancy, France

^c LEMTA, CNRS, Vandoeuvre-lès-Nancy, France

^d CMTC, CNRS/Grenoble-INP/UJF, Saint Martin d'Hères, France

ARTICLE INFO

Article history:

Received 4 December 2012

Received in revised form 27 February 2013

Accepted 5 March 2013

Available online 18 March 2013

Keywords:

Proton exchange membrane fuel cell

Platinum nanoparticles

Durability

Heterogeneities of ageing

Segmented cell

Channel and land

ABSTRACT

This paper investigates aging heterogeneities that set up during PEMFC operation in start-up and shut down conditions. The spatially-resolved analyses were based on *in situ* measurements of local current densities, electrochemical surface area of Pt at the cathode in a segmented cell and overall CO₂ generation. In complement, *ex situ* physicochemical analyses were performed after the PEMFC testing, using scanning and transmission electron microscopy as well as focused ion beam scanning electron microscopy, to probe the micro and nano-scale of the cathode catalyst layer. In the present cell configuration (counter-flow mode, impact of the shut-down events negligible versus that of start-up), two kinds of aging heterogeneities are witnessed. Firstly, the performances loss at the air outlet/H₂ inlet is less important than at the air inlet/H₂ outlet; fuel starvation events are prevalent in this latter region; the resulting local loss of performances are linked to the distribution of the internal currents along the cell, and to larger physicochemical changes of the cathode catalyst layer in the air outlet/H₂ inlet region. The faradic part of the internal currents (generated during the fuel starvation events) was identified to not only come from the electrooxidation of the carbon support of the cathode catalytic layer (CL): internal currents may also originate from Pt dissolution, carbon corrosion in the gas diffusion layer (GDL) and/or water oxidation. Secondly, the degradations at the air inlet/H₂ outlet also depend on the position during the aging, either under a channel or a land. Fuel starvation events are more pronounced in land regions, due to slower removal of oxygen trapped under a land (the source of the fuel starvation) in the anode compartment during a start-up. Finally, it is wise pointing out that the particular degradation mechanism witnessed in this study would not have been observed if the MEA had been aged following a standardized stress test (potential cycling under N₂-atmosphere); therefore, one may question whether the DOE standardized stress-test procedure is relevant to mimic real fuel cell operation.

© 2013 Elsevier B.V. All rights reserved.

1. Introduction

During the last decade, understanding the impact of environmental and operating conditions in a proton exchange membrane fuel cell (PEMFC) on the degradation rates of its platinum and

carbon based electrodes has been (and is still) crucial to develop more robust catalysts, or at least to find mitigation strategies to their degradation [1,2]. It is established that fuel cell degradation mechanisms and rates depend primarily on the PEMFC operating conditions: different phenomena leading to loss of performances occur during steady state load, potential cycling, start-up, shut-down, flooding or dry conditions [3–8].

Degradations induced by start-up/shut-down (SU/SD) have been extensively studied recently as these events, when not well-managed, are known to be the most harmful regarding the stability of the PEMFC components [8–12]. Indeed, most of the damages induced by start-up or shut-down procedures come from the simultaneous presence of oxygen (air) and hydrogen in the anode

* Corresponding author at: LEMTA, Université de Lorraine, Vandoeuvre-lès-Nancy, France. Tel.: +33 383595612.

** Corresponding author at: LEPMI – UMR5279, CNRS/Grenoble-INP/UdS/UJF, Saint Martin d'Hères, France. Tel.: +33 476826588.

E-mail addresses: Laetitia.Dubau@lepmi.grenoble-inp.fr (L. Dubau), Olivier.Lottin@univ-lorraine.fr, Lottin.Olivier@gmail.com (O. Lottin).

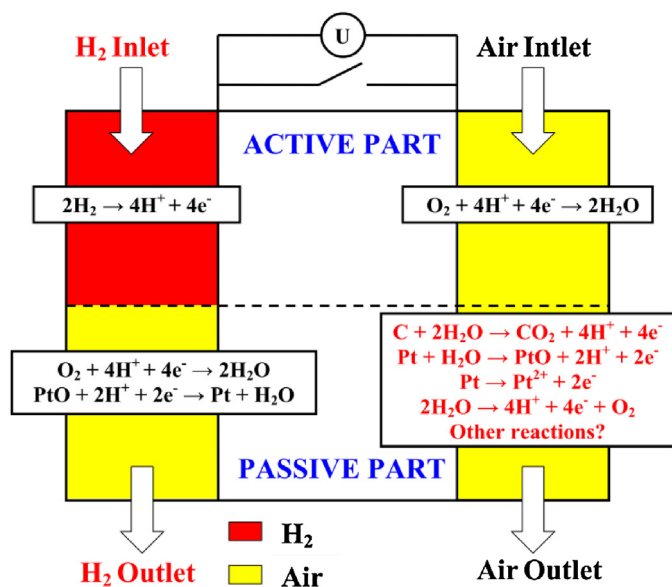


Fig. 1. Reverse currents during start-up: when injecting hydrogen in an anode compartment initially filled with air or nitrogen, the cell is temporally divided into an active part and a passive part, delimited by the hydrogen front. The active part (marked in red) operates as a fuel cell, with hydrogen oxidation at the anode and oxygen reduction at the cathode while the reverse current flows in the passive part which is not yet supplied with hydrogen. (For interpretation of the references to color in this figure legend, the reader is referred to the web version of this article.)

compartment [13]. These conditions occur for instance during hydrogen injection at start-up or when flushing the anode compartment with air at shut-down, and are commonly referred to as “Fuel starvation events” since the pioneering work of Reiser et al. [13]. They lead to higher rates of electrochemical oxidation of the materials constituting the cathode catalytic layer than under normal fuel cell operation [2,14]. Meanwhile, reverse currents, characteristic of these fuel starvation events, are generated and can be measured using segmented cells [15,16]. These reverse currents occur in the passive part of the cell (i.e., the part of the anode compartment still filled with air), while the active part (i.e., the part already filled with hydrogen) operates normally, with hydrogen oxidation at the anode and oxygen reduction at the cathode (Fig. 1). It is possible to limit the intensity of the reverse current, and thus the extent of degradation of the cathode materials, by using nitrogen instead of air to purge the anode compartment, or by connecting the fuel cell to a load [17] (although SU or SD are usually performed in open circuit). These reverse currents are more or less a marker of the degradation of the cathode CL, but their exact nature still needs to be clarified: previous studies suggested [15,16] that they could be divided into a faradic and a capacitive contribution, the order of magnitude of which being easily estimated experimentally by increasing as much as possible the hydrogen flow rate at start-up or the air/nitrogen flushing rate at shut down. However, the exact nature of the faradic contribution is not yet well understood: indeed it can include the contribution of various electrochemical oxidation reactions such as the carbon oxidation into CO_2 , surface oxide formation on carbon and platinum based materials, dissolution of platinum into its ionic form, or even water splitting into O_2 . Although extensive evidences of carbon oxidation in the cathode have been reported [18,19], we showed recently that the corresponding charge stood for only a few tenths of the faradic contribution to the reverse currents [15].

All of these contributions have led to the concept of localized phenomena: very different operating conditions (oxygen and hydrogen concentration, gas velocity, etc.) yielding very different

degradations rates of the electrodes within a distance of a few centimeters or less [18,20]. Interestingly, the accepted description of a fuel starvation event (the main source of heterogeneous degradations) has been recently refined by Schneider et al. [21]. By using a segmented cell approach based on microstructured cathode flow fields, which enable measuring the local current flowing through channel and land areas, they emphasized the effect of the flow field design on the distribution of internal currents generated during SU [21]. Indeed, at the anode side, when the fuel is reintroduced during SU, the oxygen that is located under a channel can be more or less easily removed, while it will take more time to remove the oxygen trapped under a land. Therefore, there will be longer fuel starvation events for the portion of cathode facing anode land regions than anode channel regions. This work also introduces what should be a hot topic in a near future: more than their performances [22], the degradation rates of the electrodes might be severely impacted by the design of the other components of a PEMFC unit cell (here the flow-field design of the bipolar plates and the characteristics of the gas diffusion layers).

In the present paper, the development of aging heterogeneities (between the air inlet and the air outlet) that occur during repetitive start-up and shut down events will be surveyed *in situ*. In order to make the link between aging heterogeneities and degradation heterogeneities, we will first monitor *in situ* the modification of the local performances of each segment and correlate them with local degradation of the membrane electrode assembly; in particular the cathode catalyst layers, will be characterized *ex situ* at the micro- and the nano-scale. A special care will be taken to identify every kind of aging heterogeneities within a single membrane electrode assembly (MEA) that is inlet vs. outlet and channel vs. land.

2. Experimental

2.1. Segmented cell and automated test bench

A $1\text{ cm} \times 30\text{ cm}$ segmented cell, described previously in [7,9], was used in this work. Air and hydrogen flow through five 30 cm long parallel channels ($0.7\text{ mm} \times 1\text{ mm}$ on both sides). The cathode compartment was machined in a segmented brass plate and the current was collected independently from 20 electrically insulated segments along the channel length. The anode flow-field plate was machined in a non-segmented gold-plated brass block. Hydrogen and air were fed in counter-flow in the anode and cathode compartments, respectively. In the following, the segments are numbered from 1 to 20 in the direction of the hydrogen flow, segment #1 corresponding to the air outlet/ H_2 inlet.

During operation, the local current densities were measured by 20 shunt resistors of $5\text{ m}\Omega$ each. The cell temperature was controlled using a cooling circuit and a thermostated bath. The fuel cell was operated at about 50°C and atmospheric pressure. The inlet relative humidity of all gases (nitrogen, air, and hydrogen) was close to 90%. When voltammograms were recorded, the maximum current densities were only on the order of 30 mA/segment and they were measured using Hall current sensors (see Fig. 1 in [23]). During shut downs, air was injected through the hydrogen inlet.

2.2. Samples

Membrane-electrode assemblies, prepared as coated catalyst membranes (CCM), were purchased from PaxitechTM [24]. They consist of a $25\text{ }\mu\text{m}$ XL membrane, provided by DuPontTM, sandwiched by two catalyst layers (CL) made of Pt nanoparticles supported on high surface area carbon $800\text{ m}^2\text{ g}^{-1}$ (50 wt% Pt, ref. TEC10E50E from Tanaka K.K.). The catalyst loading was $0.4\text{ mg}_{\text{Pt}}\text{ cm}^{-2}$ at the cathode and $0.2\text{ mg}_{\text{Pt}}\text{ cm}^{-2}$ at the anode. The

240 μm -thick GDL (SGL 24BC provided by SGL Carbon) were compressed to 170 μm using silicon gaskets.

2.3. Conditioning and aging procedures

During the conditioning stage, the MEA was operated during 24 h under steady state conditions ($j = 0.5 \text{ A cm}^{-2}$, saturated hydrogen and air, $s_{\text{air}} = 3$, $s_{\text{H}_2} = 1.4$, $T = 325 \text{ K}$), except for ten oxygen starvations (two sequences of five, at the beginning and at the end of the process) and two short increases of the current density up to $j = 1 \text{ A cm}^{-2}$.

The MEA was then aged, following a procedure built up to closely mimic what happens during SU/SD events. Although it is relevant to study and analyze fuel cell degradations in real use conditions (in stack or system) [25,26], the deep understanding of these most damaging working phases, and subsequently the development of efficient mitigation strategies, requires specific PEMFC designs (unit cell with small geometry) and well adapted aging protocols (also called accelerated stress tests) that can be performed in laboratory. An approach opened to criticism, but which has been extensively used in the past years. In the particular case of start-up (SU) or shut-down procedures (SD), it is however very uncertain that the accelerated stress tests commonly used, based on cycling the cathode catalyst between 0.6 V vs. RHE and 1.4 V vs. RHE in a N_2 saturated atmosphere, are relevant replica [23]. Therefore, in this study, in order to more closely mimic true SU/SD events, the aging sequence, repeated 136 times, was the following:

- (i) operation at $j = 0.5 \text{ A cm}^{-2}$ during $t = 300 \text{ s}$
- (ii) shut-down (in open circuit) by flushing the anode with (humidified) air at high velocity during 300 s (1.8 m s^{-1} equating to 20 slph)
- (iii) start-up (in open circuit) by introducing hydrogen in the anode compartment with a low velocity (0.18 m s^{-1} equating to 2 slph).

Using a high air velocity during shut-downs made it possible to limit significantly the concomitant presence (residence time) of air and hydrogen in the anode compartment and the subsequent carbon/Pt oxidation at the cathode. Indeed, the total charge passed between the active and passive parts of the cell (obtained by integrating over time the reverse currents measured in all the segments [15], this being done during start-ups as well as during shut-downs) was of about 0.75 C during shut-down with an air velocity of 1.8 m s^{-1} and 4 C during start-up with a hydrogen velocity of 0.18 m s^{-1} . Assuming that the capacitive contribution of the reverse currents is given by the asymptotic limit of the charge passed at high hydrogen or air velocity [15] (about 1 C at start-up and 0.5 C during shut-down), the faradic contribution and thus the MEA degradation rate were consequently up to twelve times lower during shut-downs than during start-ups.

In order to monitor *in situ* the MEA degradations, characterization periods were performed every 17 sequences. A characterization period included the measurement of polarization curves, galvanostatic electrochemical impedance spectra (at $j = 0.5 \text{ A cm}^{-2}$) and cyclic voltammograms. Each of these were recorded locally for each segment. In this work, cyclic voltammograms were used to estimate the platinum ElectroChemical Surface Area (ECSA) using the driven-cell mode [27]: the cathode (used as the working electrode) was first flushed with nitrogen, then the nitrogen flow was stopped and the potential was scanned from 0.1 V to 1.2 V (vs. the anode potential, which remains close to 0 V vs. RHE) at $v = 50 \text{ mV s}^{-1}$. The corresponding local current densities were recorded during the second potential scan (complementary tests showing that no significant variations occurred during the following potential scans). It was therefore possible to

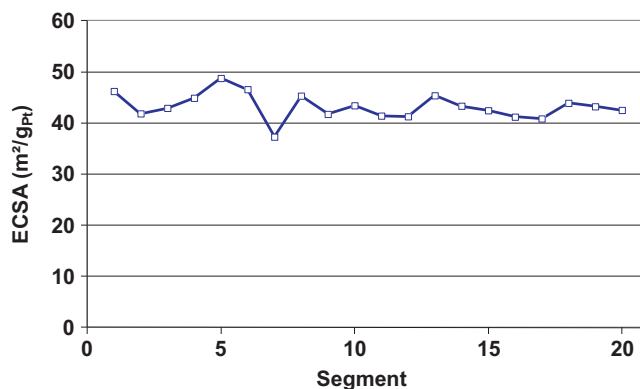


Fig. 2. Local ECSA profile measured for an MEA after the conditioning stage.

obtain the Pt ECSA profile along the MEA. Fig. 2 shows that the cathode is initially homogeneous in terms of Pt ECSA, for all segments ($43 \text{ m}^2_{\text{Pt}} \text{ g}^{-1}_{\text{Pt}} \pm 14\%$ equating to $172 \text{ cm}^2_{\text{Pt}} \text{ cm}^{-2}_{\text{MEA}}$ or $258 \text{ cm}^2_{\text{Pt}}$ per segment).

2.4. Post-aging analysis

MEA prepared by the CCM procedure enable easy post-mortem analyses of the aged catalyst [28]. The two GDL can be easily mechanically removed without detaching the catalyst layers from the membrane, leaving the catalyst layers unaltered and free of access for all the *ex situ* physical and chemical characterization techniques [29].

2.4.1. Scanning electron microscopy (SEM) observations of the MEA cross-sections

Embedded cross sections of the fresh/aged MEA were observed with a Field Emission Gun–Scanning Electron Microscopy (FEG–SEM, Zeiss Ultra 55 microscope) in order to monitor variations of the components thickness (catalytic layers and proton exchange membrane) upon aging. For the preparation of the MEA cross sections, the MEA were first embedded in Epoxy[®] resin, dried under ambient air for 1 day, polished with SiC polishing disk with small grain size (4000) and finally covered by a thin carbon film. To measure each average thickness of the MEA components, the number of pixels corresponding to each layer was integrated (with ImageJ[®]) prior to conversion to an equivalent thickness.

2.4.2. Ultramicrotomed slices preparation, STEM and TEM observations

For the preparation of the ultramicrotomed samples, small pieces (1 cm^2) of the (fresh/aged) MEA were embedded in Epoxy[®] resin and dried at $T = 333 \text{ K}$ for 3 days. Then the samples were sliced with an ultramicrotome (Leica[®] EM UC6) using a diamond knife (Diatome[®] ultra 35[°]) to obtain 70 nm-thick slices. The ultramicrotomed slices of fresh/aged membrane electrode assemblies were then deposited on a copper grid bearing a lacey carbon membrane for their observation.

Transmission electron microscopy (TEM) observations were performed with a Jeol 2010 TEM operated at 200 kV with a point to point resolution of 0.19 nm. The particle size distribution of each catalyst was reconstructed by measuring the diameter of at least 400 individual and round-shaped particles from representative TEM images obtained at high magnification ($\times 200,000$). For each particle size-distribution histogram, the number-averaged

diameter \overline{d}_N , the surface-averaged diameter \overline{d}_S , and the volume-averaged diameter \overline{d}_V were determined [30]:

$$\overline{d}_N = \frac{\sum i = 1 n l_i d_i}{\sum i = 1 n l_i} \quad (1)$$

$$\overline{d}_S = \frac{\sum i = 1 n l_i d_i^3}{\sum i = 1 n l_i d_i^2} \quad (2)$$

$$\overline{d}_V = \frac{\sum i = 1 n l_i d_i^4}{\sum i = 1 n l_i d_i^3} \quad (3)$$

l_i stands for the number of particles having a diameter d_i . Additional FEG-SEM observations, using the Scanning Transmission Electron Microscopy (STEM) mode, were performed on the ultramicrotomed samples. This microscope is designed to maximize the imaging resolution at low beam energies. The Ultra 55 is equipped with a secondary electron detector inside the lens (Inlens detector) and a backscattered electron detector. Both are engineered to image electrons at low accelerating voltage (below 5 kV), which is useful to image polymer-containing samples like PEMFC MEAs.

2.4.3. FIB-SEM observations and reconstruction of the 3D structure of the CL

In order to reconstruct the 3D structure of the pristine/aged cathode CL, and thus access to their porosity, focused ion beam (FIB)-coupled with FEG-SEM observations were performed in an automated procedure. In the imaging procedure, images at $\times 20,000$ magnification were taken with the in-lens secondary electron detector. For the milling procedure, thin lamellae (12 nm thick) of the cathode catalyst layer were removed with the focused ion beam. The automated procedure consisted of a correction drift sensor, which allowed reconstructing easily a stack of 240 images for the pristine MEA and 150 images for the aged MEA. These images were first treated using the software ImageJ® and the “Otsu threshold” algorithm to obtain a binary image [31] similar as in Zils et al. [32]. Then, the porosity was estimated with the plug-in “Voxel Counter” and the reconstruction of the 3D structure was performed with plug-in “3D Viewer” of the software ImageJ®.

3. Results and discussion

3.1. In situ evidences of the inlet vs. outlet degradation heterogeneities

The global fuel cell polarization curve, measured before and after aging, is presented in Fig. 3. The decay of performance is very significant, and in first approximation mostly due to the start-up events (the cumulated common residence time of simultaneously air and hydrogen in the anode compartment is estimated of about 800 s for a total aging time of 92,000 s including start-ups, operation at constant current density and shut-downs). The decrease of the fuel cell performance observed in Fig. 3 corresponds to heterogeneous degradations: this can be explained by considering the current density profiles measured in each of the fuel cell segments during start-up. Fig. 4 shows for instance that segment #1 and segment #20 are subjected to very different transient conditions: while segment #1 is almost instantly filled with hydrogen and delivers at once a positive internal current, segment #20 remains in contact with air on both sides during most of the start-up process. As a consequence, the internal current density flowing through segment #20 is negative, except at the very end of the start-up procedure, when the charges stored in the double layer

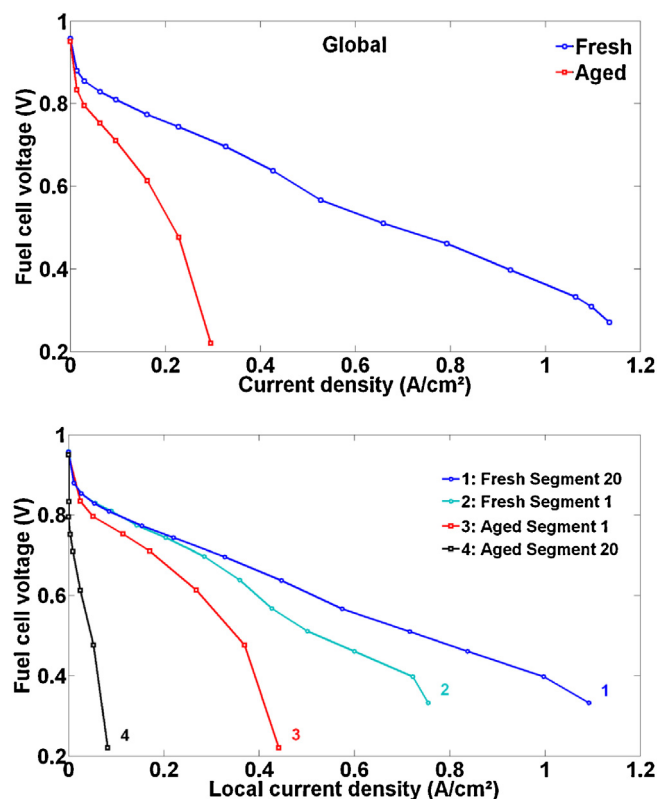


Fig. 3. Global (up) and local (down) fuel cell polarization curves after the conditioning stage and after aging. Segment 1 corresponds to cathode outlet/anode inlet; segment 20 corresponds to the cathode inlet/anode outlet (see Fig. 4).

capacities of each segment equilibrate. At this time, the current density in the segments located near the hydrogen inlet becomes slightly negative [15]. Intermediate behaviors can be observed in the segments located in the center of the cell.

The heterogeneous degradation of the MEA can be observed through the performance losses illustrated in Fig. 5, which displays the evolution of the current density profile measured when the fuel cell is operated at a constant intensity ($I = 15$ A; $j = 0.5$ A cm⁻²). First, the flat current density distribution at the beginning of the aging test confirms the initial homogeneity of the MEA (Fig. 2). Then, during the aging test, the performances of the segments located near the hydrogen outlet decrease with time. Since the fuel cell was operated at a constant intensity, the current density provided by the cathode outlet has to increase in order to compensate the local current density decrease at the cathode inlet. It must be noted that current density profiles measured after 68 SU/SD sequences do not correspond to an average current density of 0.5 A cm⁻² because the fuel cell was not able to reach 15 A anymore (dashed lines in Fig. 5). In this case, the cell supplies a current that decreases progressively from 0.47 A cm⁻² (after 85 SU/SD cycles) to 0.34 A cm⁻² (after 136 SU/SD cycles).

CO₂ emissions were measured during the fuel cell SU using a single beam Infrared multi-Component Analyzer (600 series by California Analytical Instrument, Inc.): they correspond to an overall carbon oxidation rate of about 0.2 μg cm⁻² SU⁻¹ (for the whole MEA: the CO₂ analyzer does not enable the determination of the local CO₂ emissions profile along the MEA). In addition, local cyclic voltammetry experiments performed every 17 SU/SD sequences give the evolution of the local Pt ECSA profile in the cathode (Fig. 6): the decrease is more significant for the segments located near the hydrogen outlet i.e. those which stay the longest in contact with oxygen. In opposition, the Pt ECSA of the first segments slightly

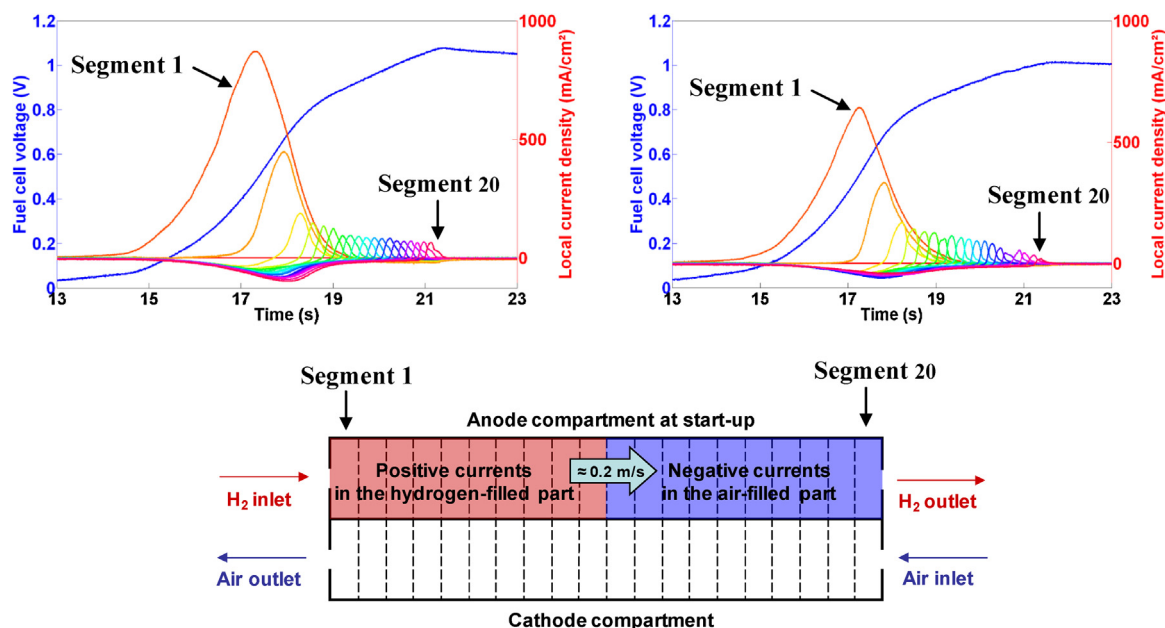


Fig. 4. Current density flowing in each segment during the 34th (left) and 136th (right) start-up (segment #1 = H₂ inlet/air outlet).

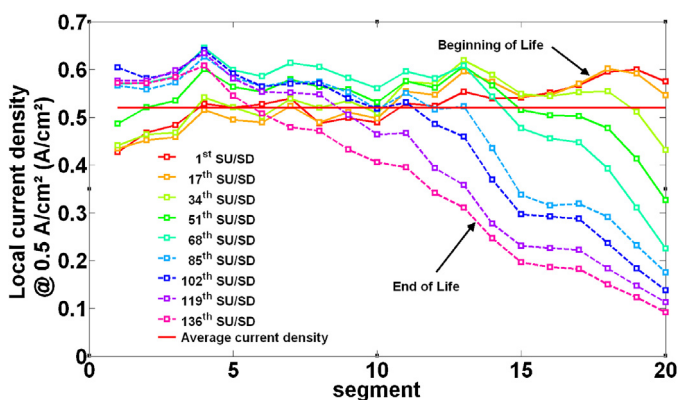


Fig. 5. Current density profiles along the air channel (segment #1 = air outlet/H₂ inlet) after the conditioning stage and during aging. The fuel cell was operated at a constant intensity of 15 A corresponding to an average current density of 0.5 A cm⁻². The profiles are represented by solid lines when the required 15 A are produced by the cell, and by dashed lines otherwise.

increases during the first SU/SD sequences and then decreases, but at a much slower rate than at cathode inlet.

3.2. Ex situ evidences of degradation heterogeneities at the micro-scale: from an inlet vs. outlet to a channel vs. land degradation issue

After the 136 SU/SD events, the segmented cell was dismantled and the MEA characterized using standardized procedures [25,33,34]. First, locally-resolved SEM observations were performed on the aged MEA as a function of the position within the segmented cell during the aging (Fig. 7B–D). While the pristine MEA (Fig. 7A) displays a uniform thickness for all its components all along the channel length ($d_{\text{cathode}} = 9.5 \pm 1 \mu\text{m}$; $d_{\text{membrane}} = 28 \pm 1 \mu\text{m}$; $d_{\text{anode}} = 4 \pm 0.5 \mu\text{m}$), the cross-sections of the aged MEA reveal that the active layers have aged heterogeneously all along the MEA length. Close to the cathode outlet, at segment #5 (Fig. 7B), the region that has operated mostly actively during the SU events, the MEA looks very similar to its pristine state ($d_{\text{cathode}} = 7 \pm 1 \mu\text{m}$; $d_{\text{membrane}} = 28 \pm 1 \mu\text{m}$; $d_{\text{anode}} = 4 \pm 0.5 \mu\text{m}$), with only a little amount of Pt crystallites precipitated as a Pt-band in the PEM. The morphology of the MEA is different when looking closer to the cathode inlet (e.g. segment #15 in Fig. 7C and segment #18 in Fig. 7D). The reduced cathode thickness ($d_{\text{cathode}} = 3 \pm 1 \mu\text{m}$) indicates that severe carbon corrosion rates have taken place in the part operating mostly passively during the SU, while no/insignificant variations of either the PEM ($d_{\text{membrane}} = 27 \pm 1 \mu\text{m}$) or the anode ($d_{\text{anode}} = 4 \pm 0.5 \mu\text{m}$) thicknesses are monitored. The decrease of the cathode thickness is concomitant with the appearance of a dense Pt-band located in the PEM, which explains part of the decrease of the ECSA recorded *in situ* in these regions of the MEA (Fig. 6). Such development of inlet vs. outlet degradation heterogeneities have already been reported to develop during accelerated aging test in cycling mode [20] and also during long-term aging when transient conditions are not well managed [3,35].

In addition, when looking with more accuracy to the segments that have aged close to the cathode inlet, another level of heterogeneity appears. Indeed, after removing the GDL from the cathode, residual portions of the micro-porous layer were left on the top of

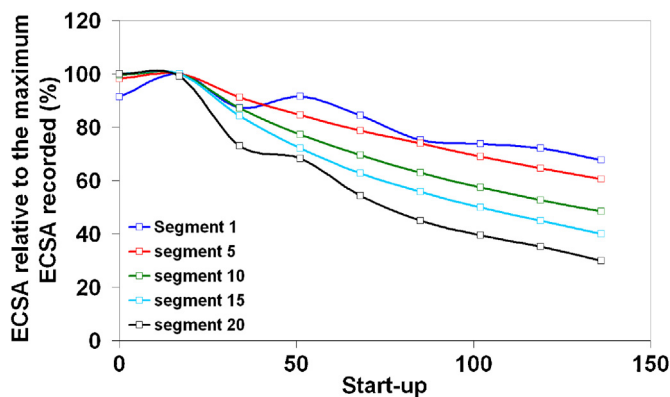


Fig. 6. Change of local Pt ECSA at the cathode of segments # 1–5–10–15–20 vs. the number of SU (segment #1 = air outlet/H₂ inlet). The initial values correspond to the data given in Fig. 2. Note that for all segments, the maximum value of ECSA was reached between the conditioning stage and the 17th SU/SD sequence.

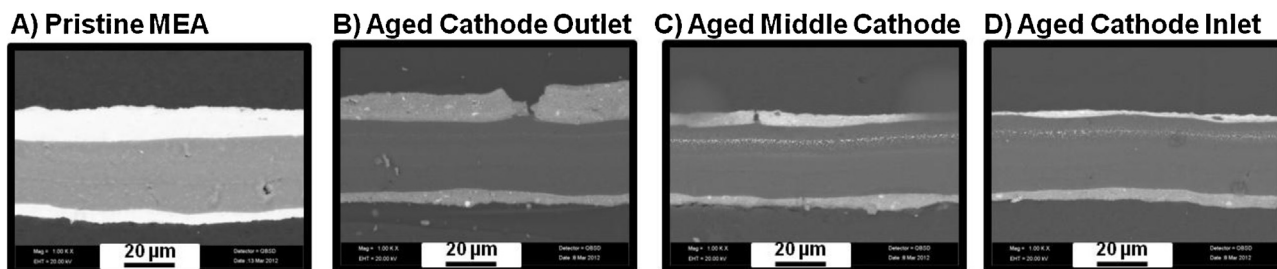


Fig. 7. SEM images recorded in back-scattered mode (magnification $\times 1000$) of (A) a pristine MEA and of (B–D) the MEA, aged under repeated 136 SU/SD cycles, taken at different locations i.e. from the cathode outlet (segment #1) to the cathode inlet (segment #20). The upper electrodes are the cathodes.

the active layer, as seen with the top view of the aged MEA (Fig. 8A). The position and dimensions of these MPL residues match with the part of the MEA that has operated under a land. The rationale for the local presence of residual portions of the MPL is open to discussion. The hypothesis of a high compression of the MEA under the channel, which would induce mechanical damages within the MEA structures, can be discarded, as this phenomenon is neither seen at the cathode outlet (segment #1), where fuel starvation events are absent, nor on the anode side. In the present study, such local degradation of the MPL was only monitored close to the cathode inlet. Therefore, such MPL residues are clearly a fingerprint of the land region, and will therefore be used in the following as a marker to enable performing locally-resolved characterization techniques.

Based on SEM images taken close to the cathode inlet, the cathode appears more degraded (at the micro-scale) under a land (Fig. 8C) than under a channel (Fig. 8B): the remaining cathode is smaller ($d_{\text{cathode}} = 3.3 \pm 0.5 \mu\text{m}$ under a land vs.

$d_{\text{cathode}} = 4.9 \pm 1.5 \mu\text{m}$ under a channel) and appears brighter, signifying the higher Pt content/lower carbon content. Interestingly, the Pt-band in the PEM is located at approximately the same position, sign of similar H_2 and O_2 partial pressure ratio under a land or under a channel [36]. Here it is also worth saying that such differences between channels and lands were not observed close to the cathode outlet, the region that has been spared from fuel starvation events.

The development of such channel vs. land heterogeneities, in regions where harsh carbon corrosion rates occur following fuel starvation events, match perfectly with the findings of Schneider and von Dahlen [21]: the portions of cathode facing an anode land region are indeed expected to suffer longer fuel starvation events than those facing anode channel regions, due to the time needed by hydrogen to diffuse below the land. As the anodic and cathodic bipolar plates are symmetric and the anodic lands face the cathodic ones in the present cell setup, faster degradation rates are

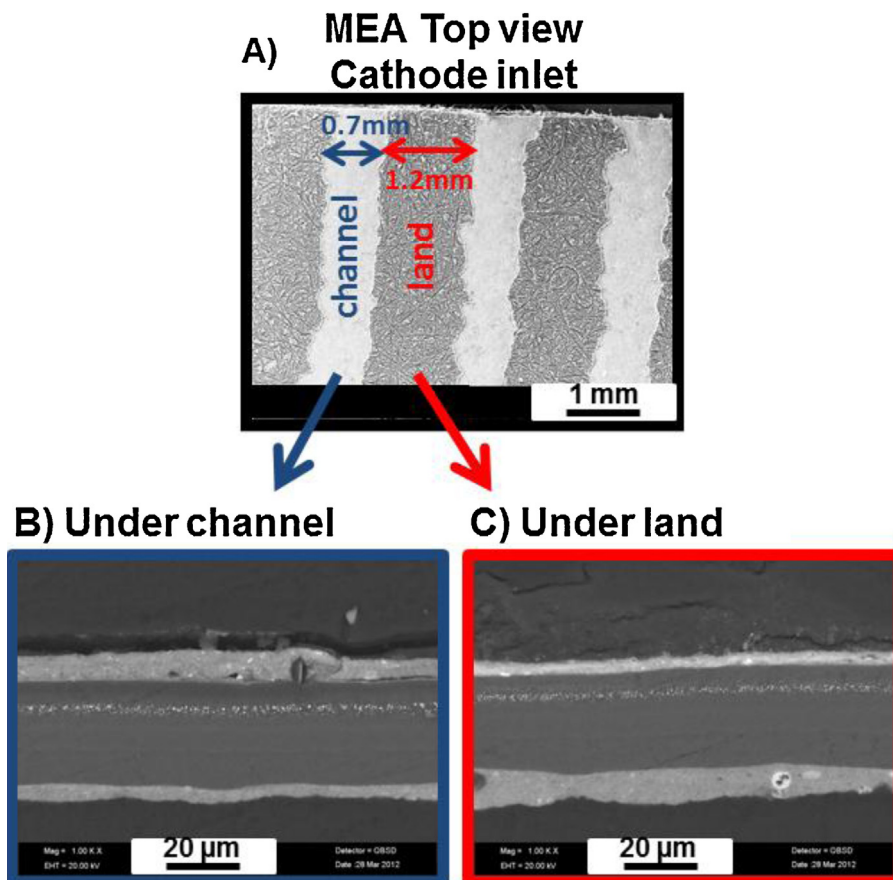


Fig. 8. SEM images in back-scattered mode of (A) the top view of the aged MEA taken under segment #18 and the cross-sections of the two distinct regions in segment #18: (B) under a channel and (C) under a land respectively. The upper electrodes in (B) and (C) are the cathodes.

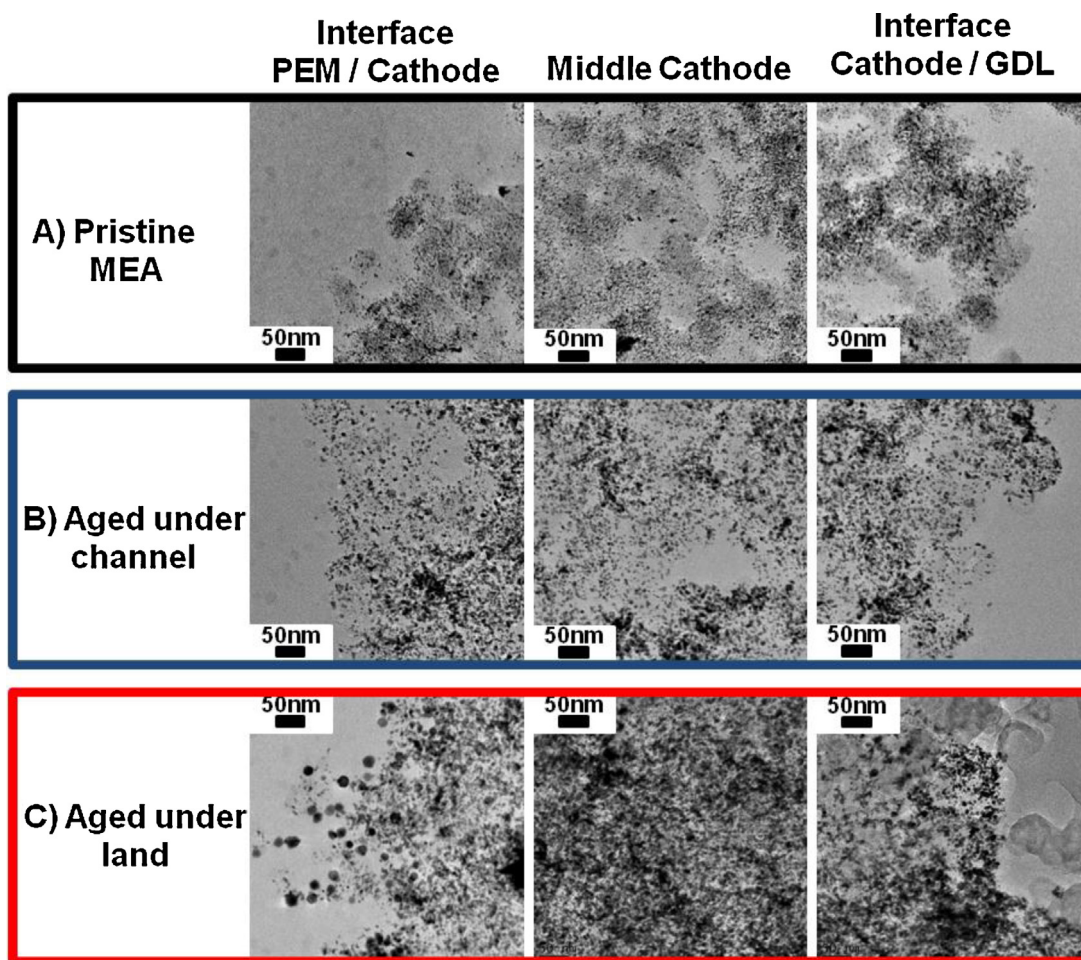


Fig. 9. TEM images of ultramicrotomed samples (magnification $\times 50,000$) taken through the cathode thickness i.e. from the PEM/cathode interface to the cathode/GDL interface, of (A) a pristine MEA and of (B and C) two samples of MEA aged at segment #18 of the segmented cell (close to the cathode inlet). The analyzed samples in (B) and (C) were aged under a channel and a land respectively.

witnessed for the land regions of the cathode. Moreover, the humidified conditions used in this study ($RH > 90\%$ and $T = 50^\circ\text{C}$) induce slower oxygen diffusion as compared with dry conditions (liquid phase vs. gas phase diffusion), therefore exacerbating channel vs. land heterogeneities [21].

Although the preliminary SEM observations of Fig. 8 clearly demonstrated heterogeneous rate of aging at the micro-scale between channel and land regions, more insights at the nano-scale are now required to identify the impact of these degradation heterogeneities on the local morphology of the Pt and C particles.

3.3. Micro to nano-scale channel vs. land degradation heterogeneities

3.3.1. Characterization of the pristine MEA

Fig. 9A displays a series of TEM micrographs taken on ultramicrotomed slices of the pristine MEA, emphasizing the fine nano-scale structure of the cathode CL. These snapshots were taken when moving from the PEM/cathode interface (on the left) to the cathode/GDL interface (on the right). The results clearly demonstrate that the pristine cathode CL is homogeneous in terms of:

to [30], agrees with Schlögl et al. measurements on the same cathode catalyst [37].

- (ii) Porosity through the cathode thickness. FIB-SEM observations performed on the pristine cathode CL enabled reconstructing the 3D electrode structure (Fig. 11A). A porosity of approximately $\varepsilon = 50\text{ vol.}\%$ is measured, which matches with previous measurements performed on similar materials by FIB-SEM [32,38–40] or other physical techniques [41]. However, assuming a bulk carbon density of approximately $\text{ca. } 2\text{ g cm}^{-3}$, a carbon loading in the electrode of $\text{ca. } 0.4\text{ mg C cm}^{-2}$ and a cathode CL thickness measured on SEM micrographs of $\text{ca. } d_{\text{cathode}} = 9.5\text{ }\mu\text{m}$, the true porosity should be much closer to $\varepsilon = 75\%$. The disparity between the often measured values and this latter figure may be attributed to the inability of SEM observations to measure the smallest pores [39], but also to difficulties to isolate only the carbonaceous material in the cutting plane of the FIB slices (in other words, the depth of field is too large in SEM) [42]. Anyway, the FIB-SEM technique still seems to be the most reliable technique to conduct a comparative study on the porosity between pristine and aged electrodes, especially when the aged electrode undergo major carbon corrosion rates, as in the present case.

3.3.2. Characterization at the nano-scale of the aged MEA

For the aged samples, as the MEA that has aged close to the cathode outlet remained unaffected at the micro-scale (Fig. 7), we first assume that it would be also the case at the nano-scale,

- (i) Pt particle size on the carbon support. The particle size distribution of the pristine cathode catalyst is displayed in Fig. 10. The volume averaged diameter ($d_v = 3\text{ nm}$), determined according

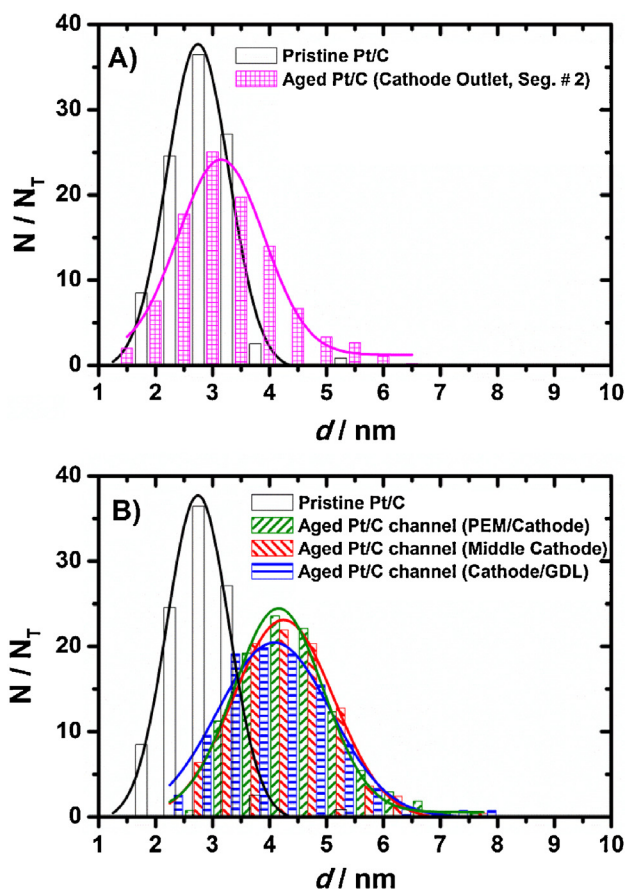


Fig. 10. Particle size distribution (PSD) of fresh (in black) and aged Pt/C catalysts, calculated based on TEM images taken at high magnification ($\times 200,000$). The PSD of the aged cathode catalyst are measured (A) close to the cathode outlet (segment #2, in pink) and (B) close to the cathode inlet (segment #18) under a channel either at the PEM/cathode interface (in green), or in the middle of the cathode (in red), or at the cathode/GDL interface (in blue). (For interpretation of the references to color in this figure legend, the reader is referred to the web version of this article.)

at least in terms of porosity of the cathode active layer. The Pt particle size distribution (PSD) of this aged cathode region is displayed in Fig. 10A. This PSD reveals a non-negligible tailing toward larger particle sizes, accompanied by a decrease of the fraction of smallest ones, with respect to the pristine catalyst. In this area, the loss of ECSA recorded *in situ* (Fig. 6) is worth 35%, i.e. from 172 to $110 \text{ cm}^2_{\text{Pt}} \text{ cm}^{-2}_{\text{MEA}}$. Assuming no changes in the

utilization factor of the MEA in this area (47% after the conditioning procedure), which may be postulated as no severe modification of the CL structure are found in this region, the overall (total) ECSA developed by the Pt/C nanoparticles should therefore decrease from 365 to $234 \text{ cm}^2_{\text{Pt}} \text{ cm}^{-2}_{\text{MEA}}$. Knowing the relative variations in the total ECSA (in $\text{m}^2_{\text{Pt}} \text{ cm}^{-2}_{\text{MEA}}$), and the relationship between the ECSA (in $\text{m}^2 \text{ g}^{-1}_{\text{Pt}}$), the mean particle size (from $d_s = 2.9 \text{ nm}$ to 3.8 nm) and the platinum density ($\rho_{\text{Pt}} = 21.45 \text{ g cm}^{-3}$):

$$\text{ECSA} = \frac{6000}{\rho_{\text{Pt}} d_s} \quad (4)$$

the Pt loading of the aged electrode in this region has therefore decreased from 0.4 to $0.34 \text{ mg}_{\text{Pt}}$ (-15%) per cm^2 of electrode. This decrease of the Pt loading is caused mainly by the redistribution of Pt^{2+} ions in the PEM through the 3D Ostwald ripening mechanism (see the sparse but still present Pt-band in the PEM in Fig. 7). It is remarkable to note that this 15% platinum mass decrease match near perfectly the amount of Pt redistributed in the PEM after fuel cell exposure to potential cycles between 0.6 V and open circuit voltage estimated by Schulenburg et al. [10]. This Pt mass loss should induce a decrease of the ECSA from $172 \text{ cm}^2_{\text{Pt}} \text{ cm}^{-2}_{\text{MEA}}$ to $145 \text{ cm}^2_{\text{Pt}} \text{ cm}^{-2}_{\text{MEA}}$. As the total ECSA experimentally decreases from $172 \text{ cm}^2_{\text{Pt}} \text{ cm}^{-2}_{\text{MEA}}$ to $110 \text{ cm}^2_{\text{Pt}} \text{ cm}^{-2}_{\text{MEA}}$ (-35% , see Fig. 6), this leaves a 20% ECSA decrease due to crystallite growth and/or agglomeration. Interestingly, the two main degradation mechanisms identified here (redistribution of Pt out of the CL vs. growth/agglomeration of the remaining Pt crystallites) impact the loss of ECSA at similar extent.

In conclusion, and to make the link with the aging procedure, the loss of ECSA in this cathode outlet region occurs *via* (i) anodic (potential steps from 0.6 V to OCV) [43,44] and/or cathodic (potential steps from OCV to 0.6 V) [45,46] Pt dissolution routes, source of Ostwald ripening, but also by (ii) minor carbon corrosion events, induced by potential stepping between 0.6 V and OCV [19,47], which will promote in a minor extent the detachment and/or the agglomeration of Pt particles. As minor carbon corrosion rates are evidenced, the occurrence of potential transients at $E > 1.4 \text{ V}$ vs. RHE in this region is discarded and confirms indirectly that this region remains undamaged by SU events.

3.3.3. Characterization of the MEA aged in cathode inlet

Fig. 9 also displays a series of TEM micrographs of ultramicrotomed slices sampled in the MEA region aged close to the cathode inlet (segment # 18). As expected from the SEM micrographs (micro-scale, Fig. 8), this region has also undergone major structural changes at the nano-scale. Like for the SEM observations,

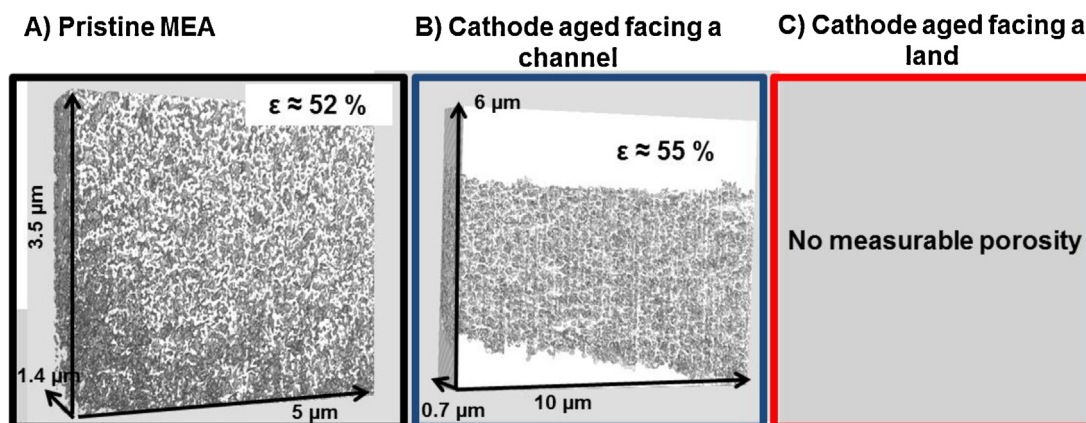


Fig. 11. Snapshots of the 3D reconstruction, using FIB-SEM, of the cathode catalyst layers (CL) of (A) the pristine MEA and of (B) the MEA aged under a channel close to the cathode inlet (segment #18).

these changes can be discussed as a function of the position during the aging, either under a channel (Fig. 9B) or a land (Fig. 9C).

In the channel region (Fig. 9B), the overall increase of the mean particle size of the catalyst is obvious. This increase seems homogeneous through-the-plane of the cathode, i.e. from the PEM|cathode interface to the cathode|GDL interface, as seen from the local particle size distribution (Fig. 10B). The mean volume-averaged diameter of the aged catalyst particles is $d_v = 4.8$ nm, whatever the location through the cathode thickness. These insignificant through-the-plane degradation heterogeneities of the cathode catalyst agree with the results found by Dubau et al. [25].

It is also interesting to compare the PSD of the cathode catalyst aged close to the cathode outlet (Fig. 10A) with that of the cathode catalyst aged close to the cathode inlet under a channel (Fig. 10B): the mean particle size is higher close to the inlet. The increased mean particle size in this area compared to the cathode outlet proves that fuel starvation events are well present under channels. However, they will proceed in a much lower extent than under lands, as will be highlighted in the following section. Actually, when looking at the CL overall structure, there seems to be minor changes of the cathode CL porosity and Pt/C morphology in this region at first sight. Indeed, the FIB-SEM experiments carried out in this specific region confirmed the minor changes in terms of the void volume (Fig. 11B) with respect to the pristine electrode.

The impact of the aging on the land regions of cathode located close to the air inlet is completely different than for channel regions in the same area, a few micrometers away. First, large Pt particles, ranking from 20 to 40 nm diameter, coexist with a high range of agglomerated particles at the PEM|cathode interface. Only agglomerated particles are found when moving toward the cathode|GDL interface. It is worth mentioning that not enough isolated Pt particles can be found throughout the cathode CL to draw accurate local or global particle size distribution (at least 400 particles are required to establish accurate statistics) similar as in Fig. 10B. All the classical degradation mechanisms leading to ECSA losses are evidenced in Figs. 9 and 10: (i) agglomeration of Pt nanoparticles upon collision due to carbon corrosion, (ii) Pt dissolution/redeposition onto larger particles within the catalytic layer, and (iii) Pt dissolution/redeposition within the PEM [48–50]. It appears difficult to distinguish which from these three contributions predominates in the loss of ECSA.

The carbon support is also severely degraded by the aging test. First, the remaining carbon support in Fig. 9C seems to be completely amorphous (all the TEM images acquired in this region appear blurred, which is a first sign of severe carbon corrosion rates [51]). The TEM images are compatible with a complete loss of porosity throughout the whole electrode thickness (Fig. 9C). This result is in agreement with the work of Carter et al., who concluded that only 10 wt.% of carbon loss is necessary to fully loose the electrode porosity [52]. Note that the $0.2 \mu\text{g cm}^{-2} \text{ SU}^{-1}$ carbon loss measured by CO_2 emissions (Section 3.1) correspond in our case to a total loss of about 0.02 mg cm^{-2} , i.e. 5% of the initial mass of carbon at the cathode (0.4 mg cm^{-2}). However, it must be kept in mind that the carbon loss is highly heterogeneous, and that the portion of solid carbon leaving the cell washed away by liquid water may be significant.

This ultramicrotomed slice of the aged MEA was also observed with a FEG-SEM in STEM mode (Fig. 12). It was striking to observe that, due to the lower electron acceleration voltage of a SEM compared to a TEM, the electron beam was not able to cross over the portion of cathode aged under a land (the electrode looks darker compared to the portion of cathode aged facing a channel). As all ultramicrotomed slices have the same thickness ($e = 70$ nm), this indirectly signs the more absorbing/dense electrode structure in the cathode aged under a land (richer in Pt/poorer in light elements such as C, F or S). This last result is partly confirmed with

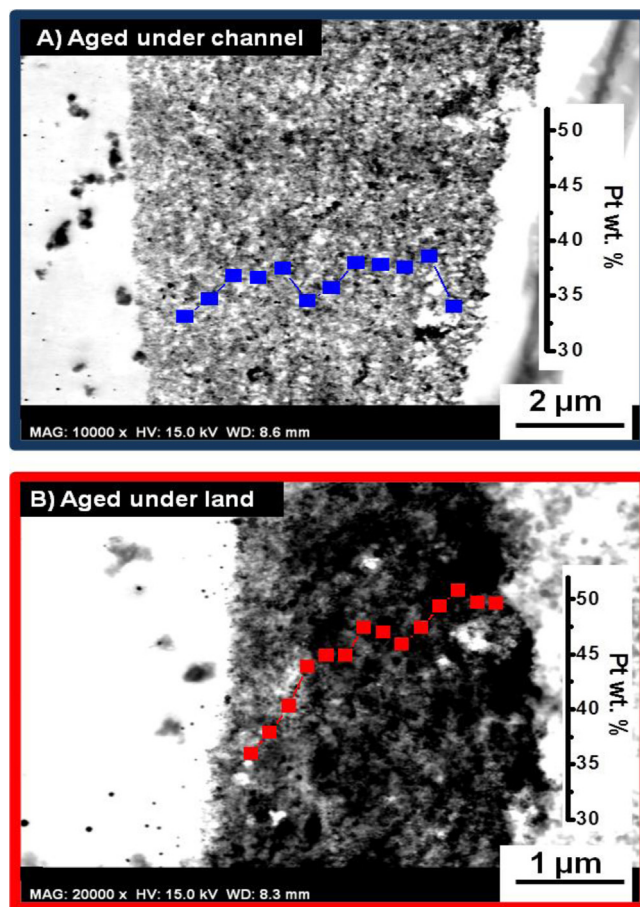


Fig. 12. FEG-SEM images recorded in STEM mode of the two MEA ultramicrotomed samples aged in segment #18 either (A) under a channel (magnification $\times 10,000$) or (B) under a land (magnification $\times 20,000$). Both PEM|cathode interfaces are located on the left of the images. The locally resolved Pt weight percent, measured with locally X-EDS analyses similar as in Dubau et al. [25], are superimposed on the FEG-SEM images. The contribution of carbon to the X-EDS signal was not considered for the calculation in the Pt weight percent.

locally-resolved X-EDS measurements, displayed over the SEM pictures (Fig. 12). The quantification of the X-EDS signal was done for the Pt, F, S and O signals, using a similar procedure as in Dubau et al. [25]. When comparing the two regions in Fig. 12, it clearly appears that the Pt content is larger in the cathode aged under a land. This confirms the higher rate of release of carbon compared to platinum from the electrode structure during multiple SU events. Thus, the electrode thickness diminishes (it becomes denser) and the Pt content remains stable overall, therefore apparently increasing when ratioed to the amount of remaining carbon. Interestingly, in the case of the region of the cathode aged under a land, the Pt content increases undoubtedly when moving from the PEM|cathode to the cathode|GDL interface, which might sign the higher carbon corrosion rates close to the cathode|GDL interface. Since fuel starvation events are rapid and intense potential disturbance events, there are reasons to believe that a distribution of the potential profile sets up through the electrode thickness during such events. Even though this hypothesis has not been verified experimentally yet, the recent development of micro-structured electrode scaffold to make spatially resolved *in situ* electrolyte potential measurements through the thickness of a PEMFC electrode may enable such measurement in a near future [53].

When combining these results with the more marked range of agglomerated and large particles, it can be concluded without doubt that this region (under a land) has experienced more carbon

corrosion during SU and SD events than (i) the cathode outlet and (ii) the neighboring part of the cathode that has been aged under a channel.

4. Conclusions

In this paper, we surveyed the development of aging heterogeneities that occur during PEMFC operation containing 136 start-up and shut down events. These aging heterogeneities, between the air outlet/H₂ inlet and the air inlet/H₂ outlet (where fuel starvation events will motivate the degradation rates of the MEA structure), were monitored *in situ* with a 30 cm² fuel cell segmented in 20 regions of similar area/shape along the flow fields. The local loss of performances of the MEA was compared to the distribution of the internal currents along the cell.

In order to have a better overview of the relation between aging heterogeneities and degradation heterogeneities, post-aging analyses of the MEA were performed using physical and chemical techniques. These characterizations were locally-resolved in order to make the link with what was measured *in situ*. In agreement with the *in situ* measurements, the part of the cathode CL aged close to the air outlet/H₂ inlet is only slightly impacted/degraded by the aging procedures, compared to the part of the cathode CL aged close to the air inlet/H₂ outlet. We have been able to identify that the faradic part of the internal currents (generated during the fuel starvation events) does not only come from the electrooxidation of the carbon support of the cathode CL, but that there are evidences that other components of the cathode CL (the Pt nanoparticles and the carbon from the MPL) participate in the development of internal currents.

The changes that have occurred at the air inlet/H₂ outlet can be discussed as a function of the position during the aging, either under a channel or a land. The observations confirmed the early predictions of Schneider and von Dahlen [21] that fuel starvation events are more marked in the portion of cathode facing a land, due to the higher difficulty to remove oxygen trapped under a land (the source of the fuel starvation) in the anode compartment during a start-up, compared to the oxygen trapped under a channel. However, the extent of degradation observed on the part of the cathode facing a channel also attests that fuel starvation events are present in this region, but in a lower magnitude. The development of aging heterogeneities between a channel and a land region is unlikely to originate from a higher compression rate of the electrodes under a land than under a channel, because no loss of the porous structure was recorded on the anode aged facing a land. However, we cannot discard any role of the compression strength in the complete loss of porosity, once the structure has been weakened by carbon corrosion, as it was proposed by Schulenburg et al. [38].

The particular degradation mechanisms evidenced in this paper on the aged MEA, and believed to happen during real fuel cell operation, would not have been seen if the MEA had been aged following a standardized stress test (potential cycling under N₂-atmosphere).

References

- [1] F.A. de Bruijn, V.A.T. Dam, G.J.M. Janssen, *Fuel Cells* 8 (2008) 3–22.
- [2] R. Borup, J. Meyers, B. Pivovar, Y.S. Kim, R. Mukundan, N. Garland, D. Myers, M. Wilson, F. Garzon, D. Wood, P. Zelenay, K. More, K. Stroh, T. Zawodzinski, J. Boncella, J.E. Mc Grath, M. Inaba, K. Miyatake, M. Hori, K. Ota, Z. Ogumi, S. Miyata, A. Nishikata, Z. Siroma, Y. Uchimoto, K. Yasuda, K.I. Kimijima, N. Iwashita, *Chemical Reviews* 107 (2007) 3904–3951.
- [3] K. Gallagher, R. Darling, T. Fuller, in: W. Vielstich, A. Lamm, H. Gasteiger (Eds.), *Handbook of Fuel Cells: Fundamentals, Technology and Applications*, vol. 6, John Wiley & Sons, 2009, pp. 819–828.
- [4] L. Dubau, J. Durst, F. Maillard, M. Chatenet, J. André, E. Rossinot, *ECS Transactions* 33 (2010) 399–405.
- [5] L. Franck-Lacaze, C. Bonnet, E. Choi, J. Moss, S. Pontvianne, H. Poirot, R. Datta, F. Lapicque, *International Journal of Hydrogen Energy* 35 (2010) 10472–10481.
- [6] J. Xie, D.L. Wood, K.L. More, P. Atanassov, R.L. Borup, *Journal of the Electrochemical Society* 152 (2005) A1011–A1020.
- [7] J. Xie, D.L. Wood, D.M. Wayne, T.A. Zawodzinski, P. Atanassov, R.L. Borup, *Journal of the Electrochemical Society* 152 (2005) A104–A113.
- [8] M.F. Mathias, R. Makharia, H. Gasteiger, J.J. Conley, T.J. Fuller, G.J. Gittleman, S.S. Kocha, D.P. Miller, C.K. Mittelsteadt, T. Xie, S.G. Yan, P.T. Yu, *Interface* 14 (2005) 24–35.
- [9] J.C. Meier, C. Galeano, I. Katsounaros, A.A. Topalov, A. Kostka, F. Schueth, K.J.J. Mayrhofer, *ACS Catalysis* 2 (2012) 832–843.
- [10] H. Schulenburg, B. Schwanitz, J. Krbanjevic, N. Linse, G.G. Scherer, A. Wokaun, *Electrochemistry Communications* 13 (2011) 921–923.
- [11] F. Ettingshausen, J. Kleemann, A. Marcu, G. Toth, H. Fuess, C. Roth, *Fuel Cells* 11 (2011) 238–245.
- [12] C. Hartnig, T.J. Schmidt, *Journal of Power Sources* 196 (2011) 5564–5572.
- [13] C.A. Reiser, L. Bregoli, T.W. Patterson, J.S. Yi, J.D.L. Yang, M.L. Perry, T.D. Jarvi, *Electrochemical and Solid-State Letters* 8 (2005) A273–A276.
- [14] C. Iojoiu, E. Guilminot, F. Maillard, M. Chatenet, J.Y. Sanchez, E. Claude, E. Rossinot, *Journal of the Electrochemical Society* 154 (2007) B1115–B1120.
- [15] A. Lamibrac, G. Maranzana, O. Lottin, J. Dillet, J. Mainka, S. Didierjean, A. Thomas, C. Moyne, *Journal of Power Sources* 196 (2011) 9451–9458.
- [16] G. Maranzana, C. Moyne, J. Dillet, S. Didierjean, O. Lottin, *Journal of Power Sources* 195 (2010) 5990–5995.
- [17] S. Didierjean, A. Lamibrac, T. Geneston, A. Rakotondrainibe, G. Maranzana, E. Rozier, F. Beille, O. Lottin, *International Journal of Hydrogen Energy* 37 (2012) 6798–6807.
- [18] W. Gu, R.N. Carter, P.T. Yu, H.A. Gasteiger, *ECS Transactions* 11 (2007) 963–973.
- [19] N. Linse, L. Gubler, G.G. Scherer, A. Wokaun, *Electrochimica Acta* 56 (2011) 7541–7549.
- [20] L. Guétaz, S. Escribano, O. Sicardy, *Journal of Power Sources* 212 (2012) 169–178.
- [21] I.A. Schneider, S. von Dahlen, *Electrochemical and Solid-State Letters* 14 (2011) B30–B33.
- [22] I.A. Schneider, M.H. Bayer, S. von Dahlen, *Journal of the Electrochemical Society* 158 (2011) B343–B348.
- [23] A. Lamibrac, G. Maranzana, J. Dillet, O. Lottin, S. Didierjean, J. Durst, L. Dubau, F. Maillard, *Energy Procedia* 29 (2012) 318–324.
- [24] Paxitech, <http://www.paxitech.com>
- [25] L. Dubau, J. Durst, F. Maillard, M. Chatenet, J. André, E. Rossinot, *Fuel Cells* 12 (2012) 188–198.
- [26] G. De Moor, C. Bas, N. Charvin, E. Moukheiber, F. Niepceon, N. Breilly, J. Andre, E. Rossinot, E. Claude, N.D. Alberola, L. Flandin, *Fuel Cells* 12 (2012) 356–364.
- [27] H.A. Gasteiger, W.B. Gu, R. Makharia, M. Mathias, B. Sompalli, in: W. Vielstich, H.A. Gasteiger, A. Lamm (Eds.), *Handbook of Fuel Cells: Fundamentals, Technology and Applications*, vol. 3, John Wiley & Sons, Chichester, 2003, pp. 593–610.
- [28] E. Guilminot, A. Corcella, F. Charlot, F. Maillard, M. Chatenet, *Journal of the Electrochemical Society* 154 (2007) B96–B105.
- [29] L. Dubau, F. Maillard, M. Chatenet, J. André, E. Rossinot, *Electrochimica Acta* 56 (2010) 776–783.
- [30] S. Trasatti, O.A. Petrii, *Journal of Electroanalytical Chemistry* 327 (1992) 353–376.
- [31] N. Otsu, *IEEE Transactions on Systems, Man and Cybernetics* 9 (1979) 62–66.
- [32] S. Zils, M. Timpel, T. Arlt, A. Wolz, I. Manke, C. Roth, *Fuel Cells* 10 (2010) 966–972.
- [33] L. Dubau, F. Maillard, M. Chatenet, L. Guétaz, J. André, E. Rossinot, *Journal of the Electrochemical Society* 157 (2010) B1887–B1895.
- [34] F. Maillard, L. Dubau, J. Durst, M. Chatenet, J. André, E. Rossinot, *Electrochemistry Communications* 12 (2010) 1161–1164.
- [35] F. Ettingshausen, J. Kleemann, M. Michel, M. Quintus, H. Fuess, C. Roth, *Journal of Power Sources* 194 (2009) 899–907.
- [36] J. Zhang, B.A. Litteer, W. Gu, H. Liu, H.A. Gasteiger, *Journal of the Electrochemical Society* 154 (2007) B1006–B1011.
- [37] K. Schlögl, M. Hanzlik, M. Arenz, *Journal of the Electrochemical Society* 159 (2012) B677–B682.
- [38] H. Schulenburg, B. Schwanitz, N. Linse, G.G. Scherer, A. Wokaun, J. Krbanjevic, R. Grothausmann, I. Manke, *Journal of Physical Chemistry C* 115 (2011) 14236–14243.
- [39] S. Thiele, R. Zengerle, C. Ziegler, *Nano Research* 4 (2011) 849–860.
- [40] C. Ziegler, S. Thiele, R. Zengerle, *Journal of Power Sources* 196 (2011) 2094–2097.
- [41] A. Fischer, J. Jindra, H. Wendt, *Journal of Applied Electrochemistry* 28 (1998) 277–282.
- [42] K.J. Lange, H. Carlsson, I. Stewart, P.-C. Sui, R. Herring, Djilali, *Electrochimica Acta* 85 (2012) 322–331.
- [43] R.M. Darling, J.P. Meyers, *Journal of the Electrochemical Society* 150 (2003) A1523–A1527.
- [44] S.G. Rinaldo, J. Stumper, M. Eikerling, *Journal of Physical Chemistry C* 114 (2010) 5773–5785.
- [45] M. Umeda, Y. Kuwahara, A. Nakazawa, M. Inoue, *Journal of Physical Chemistry C* 113 (2009) 15707–15713.
- [46] D.C. Johnson, D.T. Napp, S. Bruckenstein, *Electrochimica Acta* 15 (1970) 1493–1509.
- [47] B. Vion-Dury, Ph.D Thesis, University of Grenoble, 2011.

- [48] E. Guilminot, A. Corcella, M. Chatenet, F. Maillard, F. Charlot, G. Berthomé, C. Iojoiu, J.Y. Sanchez, E. Rossinot, E. Claude, *Journal of the Electrochemical Society* 154 (2007) B1106–B1114.
- [49] P.J. Ferreira, G.J. La O', Y. Shao-Horn, D. Morgan, R. Makharia, S. Kocha, H.A. Gasteiger, *Journal of the Electrochemical Society* 152 (2005) A2256–A2271.
- [50] Y. Shao-Horn, W. Sheng, S. Chen, P. Ferreira, E. Holby, D. Morgan, *Topics in Catalysis* 46 (2007) 285–305.
- [51] K.L. More, K.A. Perry, M. Chi, K.S. Reeves, Carbon Support Structural Degradation Observed in Aged PEM Fuel Cells, 218th ECS Meeting, Las Vegas, USA, 2010, Abstract # 611.
- [52] R.N. Carter, W.B. Gu, B. Brady, P.T. Yu, K. Subramanian, H.A. Gasteiger, in: W. Vielstich, H.A. Gasteiger, H. Yokokawa (Eds.), *Handbook of Fuel Cells: Fundamentals, Technology and Applications*, vol. 6, John Wiley & Sons, Chichester, 2009, p. 829.
- [53] K.C. Hess, W.K. Epting, S. Litster, *Analytical Chemistry* 83 (2011) 9492–9498.